Supporting Information

Tuning Guest Cations to Liberate Pore Space for Efficient C4 Hydrocarbon Separation

Xue Zhang,†[a] Tao Zhang,†[a] Miao Zeng,[a] Puxu Liu,[a] Su-Hang Wang,[a] Yu Wang*[a] and Kai-Jie Chen*[a]

[a] Key Laboratory of Special Functional and Smart Polymer Materials of Ministry of Industry and Information Technology, Xi'an Key Laboratory of Functional Organic Porous Materials, School of Chemistry and Chemical Engineering, Northwestern Polytechnical University, Xi'an, Shaanxi, China

∗ Corresponding author. E-mail addresses: wychem@nwpu.edu.cn (Y. Wang) and ckjiscon@nwpu.edu.cn (K. -J. Chen)

†These authors contributed equally to this work.

Table of contents

S3 Supplementary tables

Table S1 The physical properties of C4 olefins and paraffins.

Table S2 Separation performance comparison for materials at 298 K and 50 kPa.

Table S3 Comparison of uptake capacity and uptake selectivity of various adsorbents for C_4H_6/*n*-C_4H_8/*iso*-C_4H_8 at 298 K and 100 kPa.

References

S1 Supplementary methods

1 Ideal Adsorbed Solution Theory Calculations (IAST)

The Ideal Adsorbed Solution Theory (IAST) selectivity was calculated via the IAST++ software package. Specifically, the Dual-Site Langmuir-Freundlich (DSLF) adsorption model was employed to fit the adsorption isotherms of component 1 and component 2 on the samples at 298 K and 313 K. The optimized model fitting parameters were subsequently imported into IAST++ to compute the IAST selectivity of the equimolar (0.5/0.5) component 1/component 2 binary mixture at the same temperature. The employed model equation is shown in equation (1):

$$n(x) = q_1 \frac{(k_1 x)^{n_1}}{1+(k_1 x)^{n_1}} + q_2 \frac{(k_2 x)^{n_2}}{1+(k_2 x)^{n_2}} \qquad (1)$$

Where $n(x)$ is the quantity adsorbed (mmol/g) at pressure x, and q_1 and q_2 is the saturation loadings for component 1 and component 2 (mmol/g). k_1 and k_2 represents the fitted constant, and x represents the pressure of bulk gas at equilibrium with adsorbed phase (kPa). The n_1 and n_2 represents the Freundlich exponent.

The equation for IAST selectivity is given by equation (2):

$$S_{abs} = \frac{q_1/q_2}{p_1/p_2} \qquad (2)$$

2 Isosteric heat of adsorption

At 298 K and 313 K, the Virial equation incorporated with temperature-independent parameters a_i and b_j was utilized to quantify the adsorption enthalpies of component 1 and component 2 within samples **1** and **1·K**.

$$\ln P = \ln N + {}^{1}/_{k} \sum_{i=0}^{m} a_i N_j + \sum_{j=0}^{n} b_j N_j \qquad (3)$$

Here, P is the pressure expressed in kPa, N is the amount absorbed in mmol g^{-1}, k is the temperature in K, a_i and b_j are Virial coefficients, and m as well as n represent the number of coefficients required to adequately describe the isotherms. The values of

the Virial coefficients a_0 through a_m were then used to calculate the isosteric heat of absorption using the following expression:

$$Q_{st} = -R \sum_{i=0}^{m} a_i N_i \qquad (4)$$

Q_{st} represents the coverage-dependent isosteric heat of adsorption (kJ mol^{-1}) and R is the universal gas constant. Based on the adsorption isotherms measured by BELSORP MAX II apparatus, the heat enthalpy of *iso*-C_4H_{10}, *n*-C_4H_8, *iso*-C_4H_8 and C_4H_6 for samples **1** and **1·K** were determined at 298 K and 313 K.

3 Grand Canonical Monte Carlo (GCMC) simulation

The host-guest interactions were calculated using the Material Studio software package. Before the Grand Canonical Monte Carlo (GCMC) simulations, the guest molecules *iso*-C_4H_{10}, *n*-C_4H_8, *iso*-C_4H_8, and C_4H_6 were geometrically optimized using the Dmol^3 method[1] and the electrostatic potential (ESP) charges were applied to the guest molecules. The simulation model of the frameworks **1** and **1·K** were built from the crystal information file (CIF) adapted from the Cambridge Crystallographic Data Centre https://www.ccdc.cam.ac.uk/ via index of CCDC-1551768. To construct the simulation box of **1** and **1·K**, the original CIF file was modefied by removing the guests inside the pores and only the framework was preserved. Then 32 $H_2NMe_2^+$ or 32 K^+ cations were loaded within the framwork respaecively and geometrically optimized, the resulting host-guset structures were noted as **1** and **1·K**. Then the Q_{eq} fitted charges were applied to the framework for the following simulation.

The Grand Canonical Monte Carlo (GCMC) simulations were performed using the Sorption module. The simulation box was set up as a 1×1×1 supercell, and both the framework and the guest molecules were treated as rigid bodies and set to *P*1. The Metropolis method[2] was applied to perform the GCMC simulations. The gas–framework interaction and the gas-gas interaction were described by the standard Universal force field.[3] The loading steps, equilibration steps, and production steps were all set to 2.0×10^7. The saturation/maximum uptakes were modeled at 298 K using the

fixed-pressure task with 1.0×10^5 equilibration steps, followed by 2.0×10^7 production steps to calculate the ensemble averages. The first favorable adsorption sites were simulated by the Locate task with one guest molecule and the Fixed loading task was applied to envaluate the adsorption enthalpy at 298 K.

S2 Supplementary figures

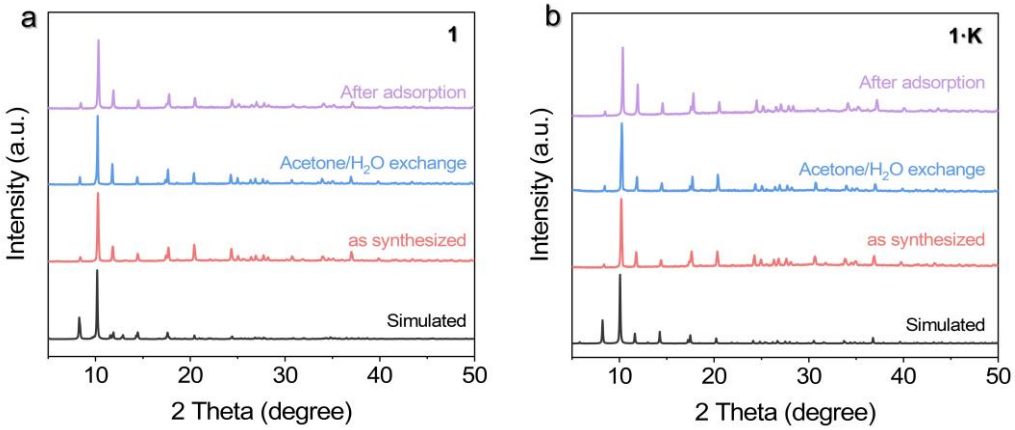

Fig. S1 The PXRD patterns of (a) **1** and (b) **1·K**.

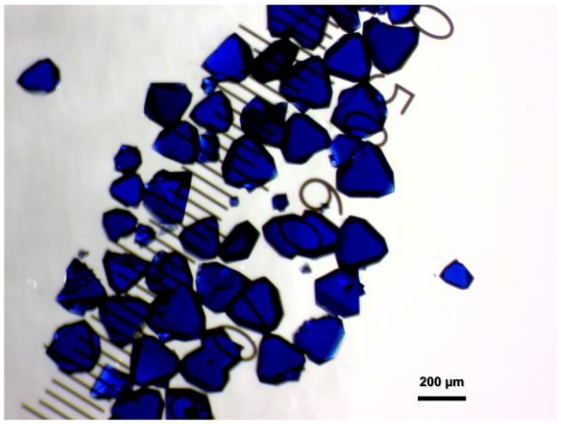

Fig. S2 The optical microscope image of **1**.

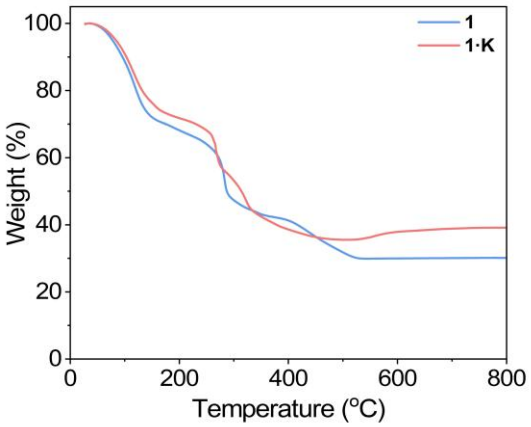

Fig. S3 TGA curves for **1** and **1·K**.

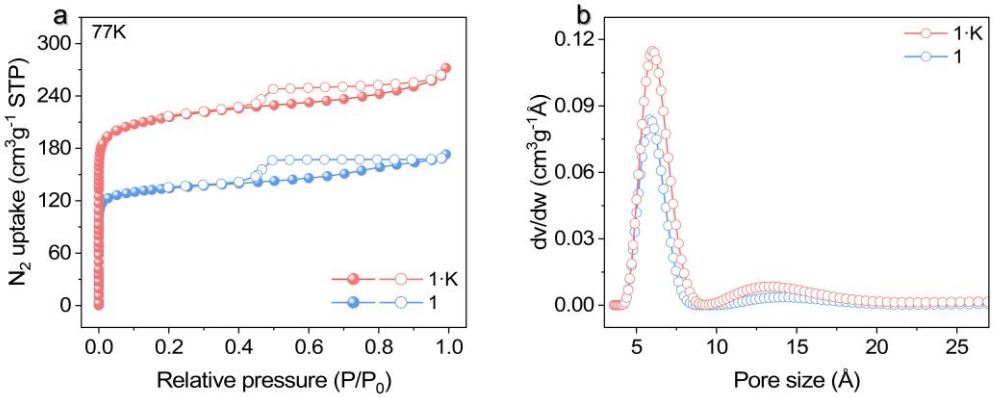

Fig. S4 The 77 K-N_2 adsorption isotherms (a) and pore size distribution (b) for **1** and **1·K**.

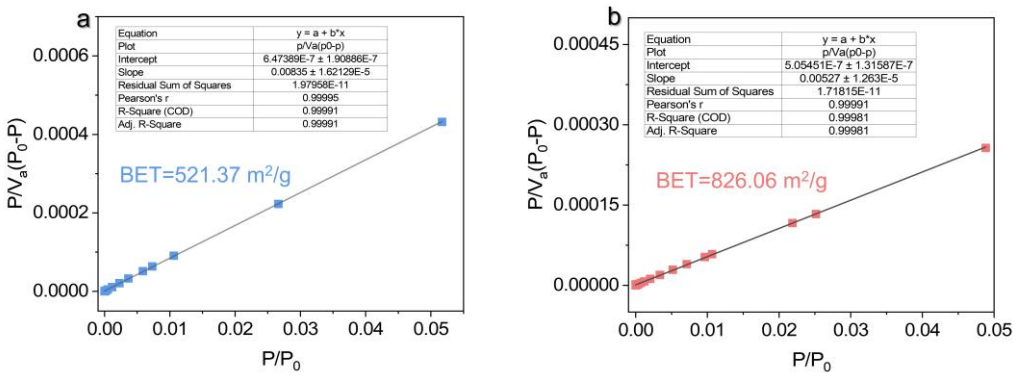

Fig. S5 The BET plots for **1** (a) and **1**·**K** (b) obtained from the N_2 adsorption isotherm at 77 K.

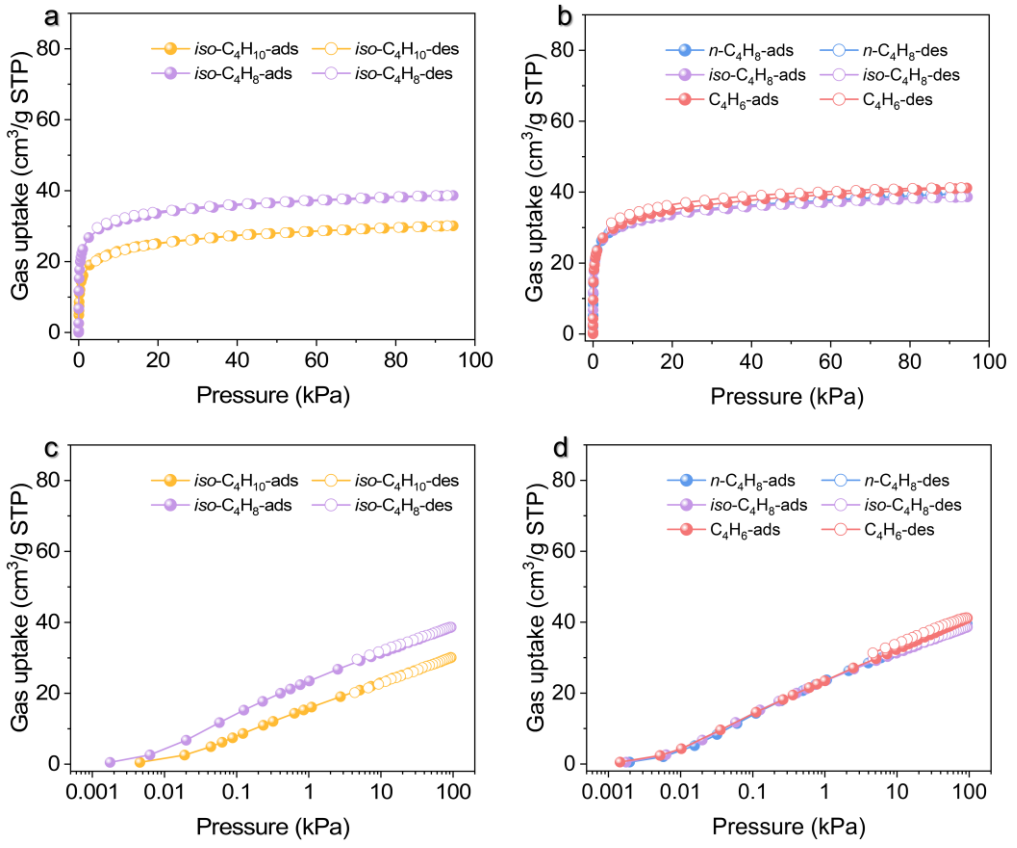

Fig. S6 The 313 K adsorption and desorption isotherms of **1** for (a) *iso*-C_4H_{10} and *iso*-C_4H_8 and (b) *n*-C_4H_8, *iso*-C_4H_8 and C_4H_6. The adsorption and desorption isotherms in logarithmic form (c, d).

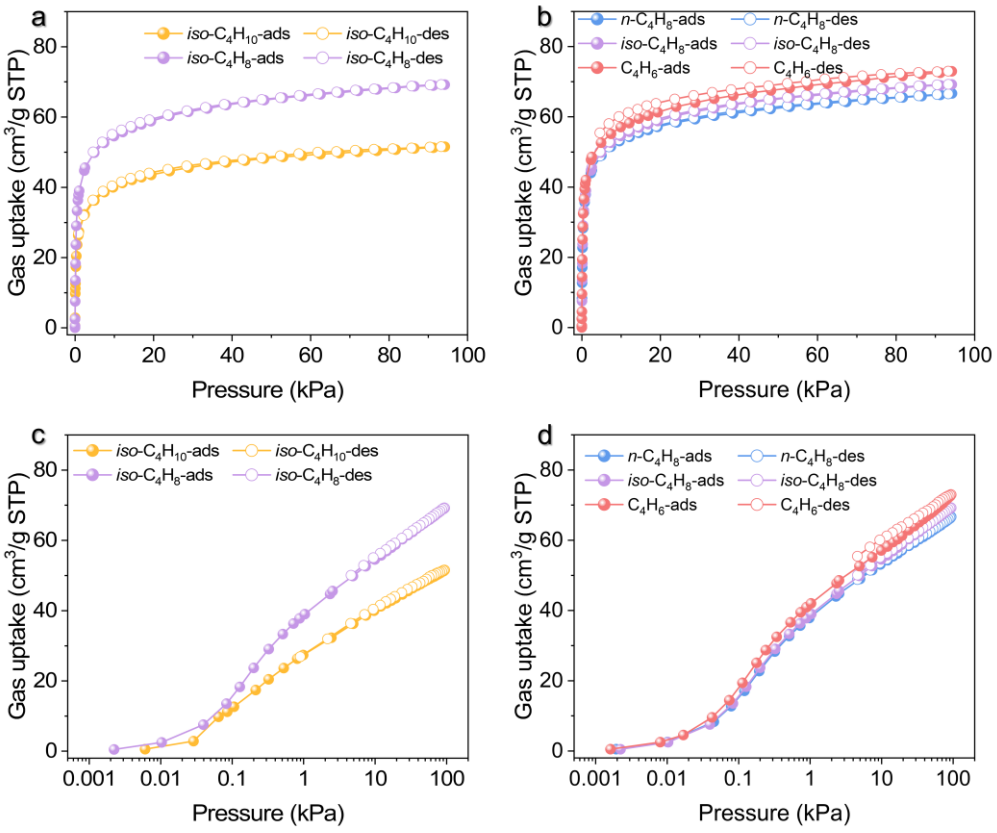

Fig. S7 The 313 K adsorption and desorption isotherms of **1·K** for (a) *iso*-C_4H_{10} and *iso*-C_4H_8 and (b) *n*-C_4H_8, *iso*-C_4H_8 and C_4H_6. The adsorption and desorption isotherms in logarithmic form (c, d).

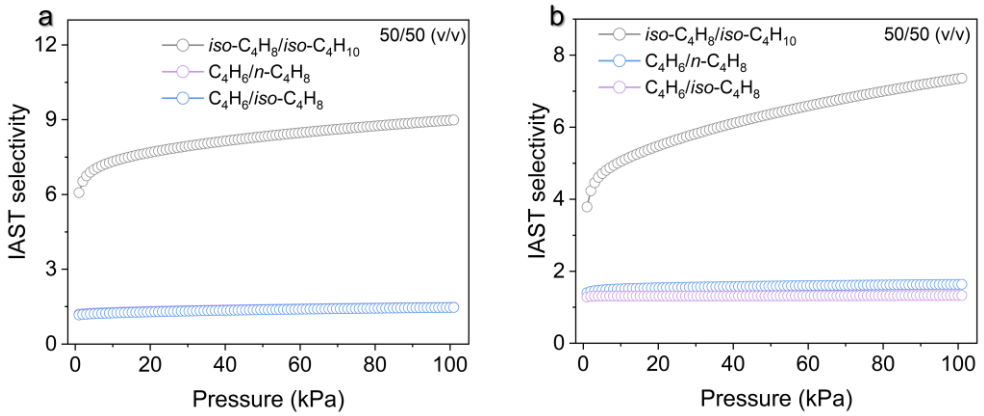

Fig. S8 IAST selectivities of **1** and **1·K** for equimolar C4 gas at 298 K (a, b).

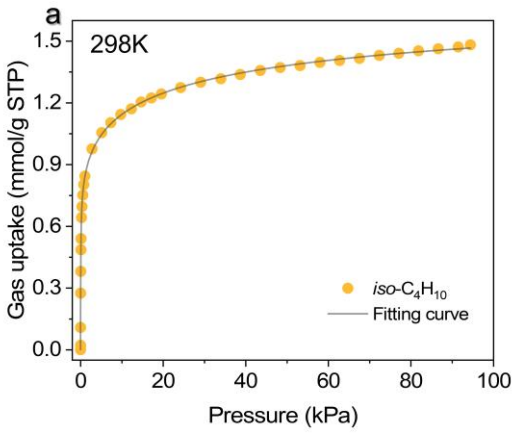

Model	DSLF (User)
Equation	q1*(k1*x)^n1/[1+(k1*x)^n1]+q2*(k2*x)^n2/[1+(k2*x)^n2]
q1	0.59936 ± 0.1158
k1	19.85607 ± 1.45345
n1	1.0814 ± 0.15056
q2	1.25845 ± 0.22909
k2	0.05699 ± 0.00984
n2	0.47302 ± 0.09006
Reduced Chi-Sqr	7.76053E-5
R-Square (COD)	0.99968
Adj. R-Square	0.99962

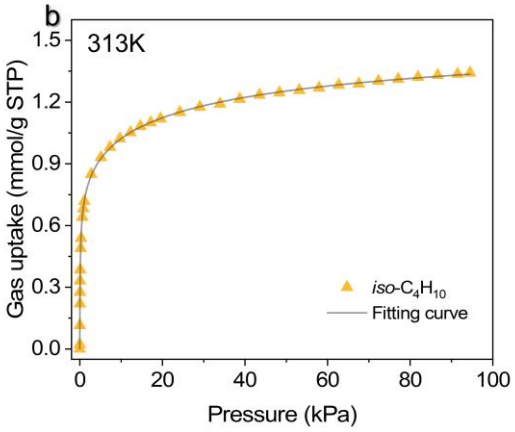

Model	DSLF (User)
Equation	q1*(k1*x)^n1/[1+(k1*x)^n1]+q2*(k2*x)^n2/[1+(k2*x)^n2]
q1	0.55818 ± 0.12606
k1	9.74474 ± 1.07543
n1	0.98816 ± 0.12582
q2	1.10779 ± 0.21266
k2	0.05509 ± 0.00983
n2	0.51816 ± 0.09671
Reduced Chi-Sqr	3.43118E-5
R-Square (COD)	0.99984
Adj. R-Square	0.99981

Fig. S9 Dual-Site Langmuir-Freundlich (DSLF) model fitting of the *iso*-C_4H_{10} isotherm of **1** at 298 K and 313 K.

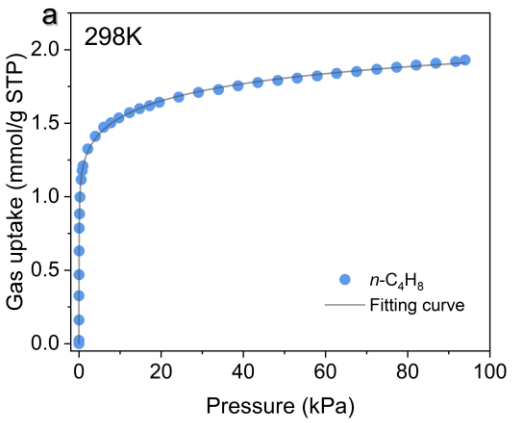

Model	DSLF (User)
Equation	q1*(k1*x)^n1/[1+(k1*x)^n1]+q2*(k2*x)^n2/[1+(k2*x)^n2]
q1	1.60033 ± 0.5843
k1	0.03011 ± 0.01751
n1	0.42077 ± 0.15217
q2	0.93797 ± 0.21925
k2	35.85433 ± 3.95874
n2	0.9284 ± 0.14684
Reduced Chi-Sqr	2.36794E-4
R-Square (COD)	0.99939
Adj. R-Square	0.9993

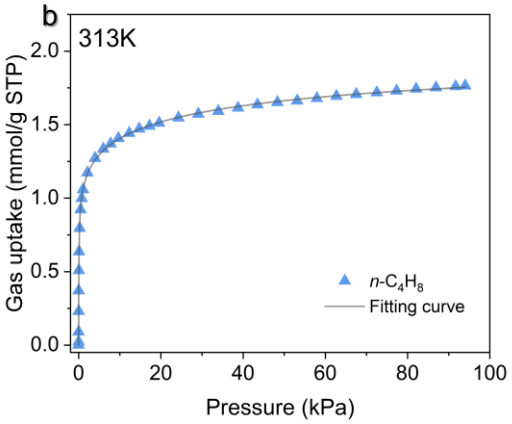

Model	DSLF (User)
Equation	q1*(k1*x)^n1/[1+(k1*x)^n1]+q2*(k2*x)^n2/[1+(k2*x)^n2]
q1	0.84363 ± 0.21149
k1	15.93899 ± 2.12557
n1	0.9292 ± 0.13702
q2	1.32062 ± 0.37042
k2	0.05597 ± 0.01441
n2	0.48082 ± 0.13214
Reduced Chi-Sqr	1.09606E-4
R-Square (COD)	0.9997
Adj. R-Square	0.99965

Fig. S10 Dual-Site Langmuir-Freundlich (DSLF) model fitting of the *n*-C_4H_8 isotherm of **1** at 298 K and 313 K.

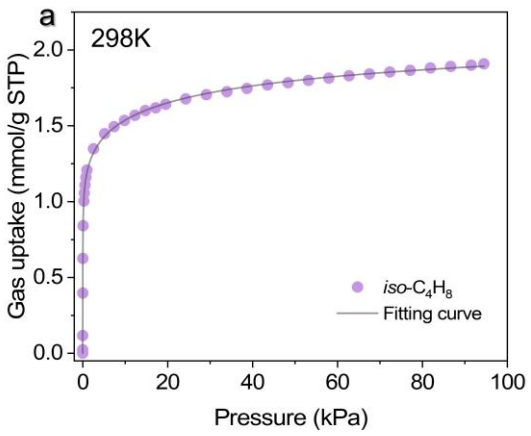

Model	DSLF (User)
Equation	q1*(k1*x)^n1/[1+(k1*x)^n1]+q2*(k2*x)^n2/[1+(k2*x)^n2]
q1	1.5234 ± 0.38033
k1	0.06335 ± 0.01639
n1	0.43041 ± 0.11438
q2	0.85093 ± 0.18095
k2	45.4038 ± 4.06116
n2	1.04867 ± 0.18277
Reduced Chi-Sqr	2.22249E-4
R-Square (COD)	0.99941
Adj. R-Square	0.99931

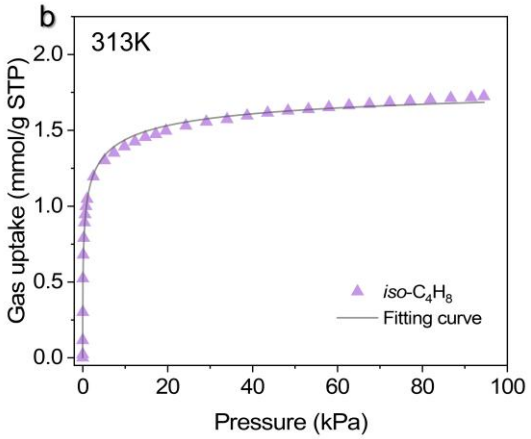

Model	DSLF (User)
Equation	q1*(k1*x)^n1/[1+(k1*x)^n1]+q2*(k2*x)^n2/[1+(k2*x)^n2]
q1	1.09686E-16 ± 0
k1	6.71452 ± 0
n1	1.79088E-8 ± 0
q2	1.88324 ± 0.04689
k2	1.52324 ± 0.24997
n2	0.42993 ± 0.02478
Reduced Chi-Sqr	0.00198
R-Square (COD)	0.99393
Adj. R-Square	0.99289

Fig. S11 Dual-Site Langmuir-Freundlich (DSLF) model fitting of the *iso*-C_4H_8 isotherm of **1** at 298 K and 313 K.

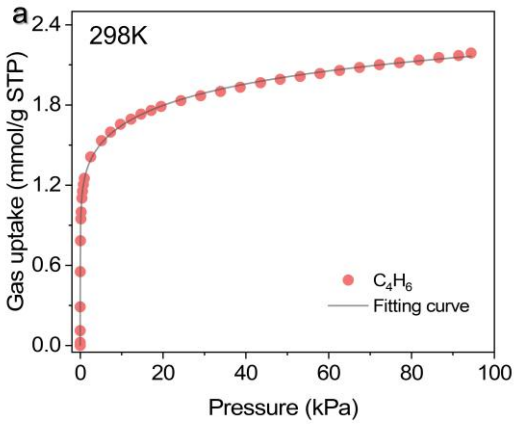

Model	DSLF (User)
Equation	q1*(k1*x)^n1/[1+(k1*x)^n1]+q2*(k2*x)^n2/[1+(k2*x)^n2]
q1	2.42528 ± 1.05164
k1	0.01218 ± 0.01451
n1	0.39875 ± 0.14981
q2	0.91794 ± 0.2524
k2	39.71894 ± 5.47246
n2	0.89385 ± 0.17824
Reduced Chi-Sqr	3.13503E-4
R-Square (COD)	0.99938
Adj. R-Square	0.99928

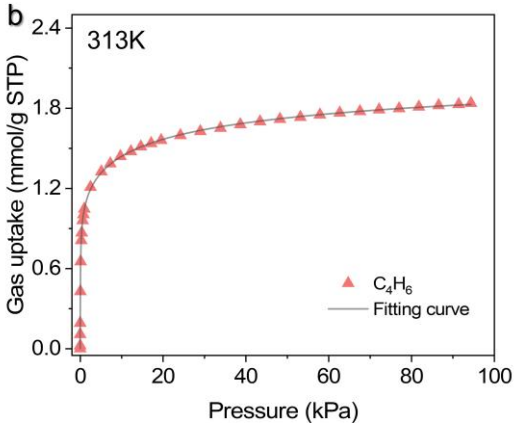

Model	DSLF (User)
Equation	q1*(k1*x)^n1/[1+(k1*x)^n1]+q2*(k2*x)^n2/[1+(k2*x)^n2]
q1	0.74488 ± 0.16772
k1	21.13663 ± 2.5268
n1	0.94469 ± 0.13194
q2	1.52573 ± 0.286
k2	0.07016 ± 0.01309
n2	0.47396 ± 0.08853
Reduced Chi-Sqr	7.79799E-5
R-Square (COD)	0.9998
Adj. R-Square	0.99977

Fig. S12 Dual-Site Langmuir-Freundlich (DSLF) model fitting of the C_4H_6 isotherm of **1** at 298 K and 313 K.

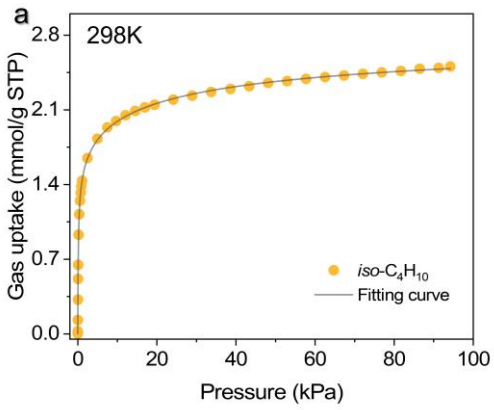

Model	DSLF (User)
Equation	q1*(k1*x)^n1/[1+(k1*x)^n1]+q2*(k2*x)^n2/[1+(k2*x)^n2]
q1	1.78072 ± 0.26786
k1	0.0882 ± 0.02297
n1	0.53661 ± 0.07237
q2	1.13874 ± 0.1938
k2	8.04241 ± 0.59882
n2	1.09528 ± 0.11575
Reduced Chi-Sqr	1.28968E-4
R-Square (COD)	0.99983
Adj. R-Square	0.9998

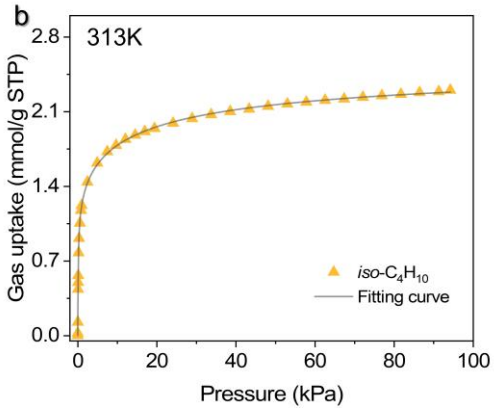

Model	DSLF (User)
Equation	q1*(k1*x)^n1/[1+(k1*x)^n1]+q2*(k2*x)^n2/[1+(k2*x)^n2]
q1	1.74167 ± 0.38349
k1	0.10371 ± 0.03275
n1	0.58115 ± 0.12787
q2	0.9064 ± 0.26394
k2	8.83461 ± 1.02657
n2	1.26513 ± 0.25304
Reduced Chi-Sqr	3.74875E-4
R-Square (COD)	0.99941
Adj. R-Square	0.99931

Fig. S13 Dual-Site Langmuir-Freundlich (DSLF) model fitting of the *iso*-C_4H_{10} isotherm of **1·K** at 298 K and 313 K.

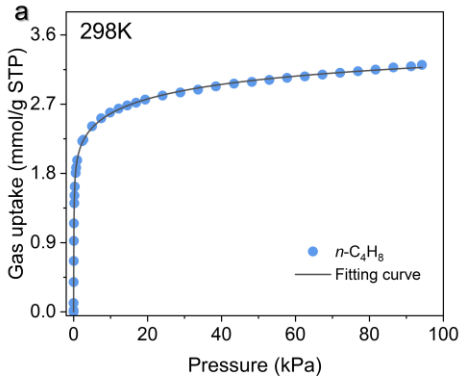

Model	DSLF (User)
Equation	q1*(k1*x)^n1/[1+(k1*x)^n1]+q2*(k2*x)^n2/[1+(k2*x)^n2]
q1	2.40179 ± 0.25357
k1	0.04772 ± 0.01015
n1	0.45516 ± 0.04843
q2	1.58106 ± 0.13715
k2	13.28082 ± 0.50806
n2	1.14842 ± 0.08017
Reduced Chi-Sqr	2.63808E-4
R-Square (COD)	0.99977
Adj. R-Square	0.99973

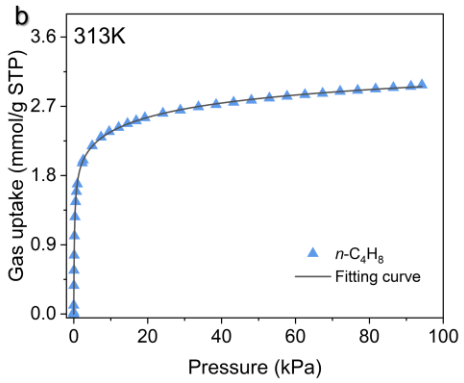

Model	DSLF (User)
Equation	q1*(k1*x)^n1/[1+(k1*x)^n1]+q2*(k2*x)^n2/[1+(k2*x)^n2]
q1	1.51641 ± 0.10276
k1	5.80055 ± 0.18432
n1	1.11771 ± 0.05278
q2	2.15063 ± 0.15495
k2	0.04483 ± 0.00784
n2	0.49051 ± 0.03307
Reduced Chi-Sqr	8.58094E-5
R-Square (COD)	0.99992
Adj. R-Square	0.99991

Fig. S14 Dual-Site Langmuir-Freundlich (DSLF) model fitting of the *n*-C_4H_8 isotherm of **1·K** at 298 K and 313 K.

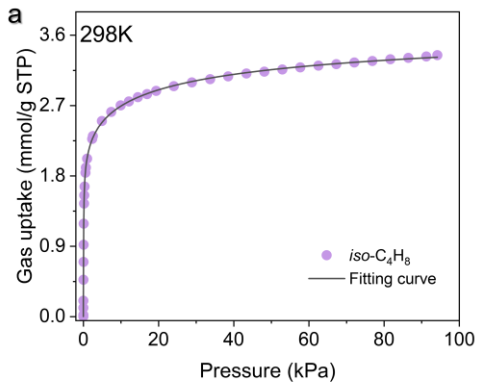

Model	DSLF (User)
Equation	q1*(k1*x)^n1/[1+(k1*x)^n1]+q2*(k2*x)^n2/[1+(k2*x)^n2]
q1	1.45689 ± 0.09775
k1	14.73407 ± 0.45006
n1	1.21416 ± 0.0694
q2	2.55685 ± 0.14513
k2	0.08766 ± 0.01234
n2	0.4657 ± 0.02603
Reduced Chi-Sqr	1.658E-4
R-Square (COD)	0.99988
Adj. R-Square	0.99986

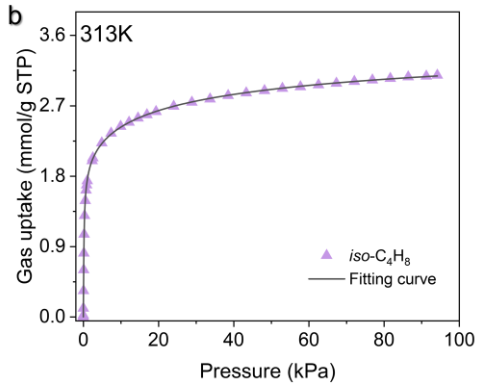

Model	DSLF (User)
Equation	q1*(k1*x)^n1/[1+(k1*x)^n1]+q2*(k2*x)^n2/[1+(k2*x)^n2]
q1	2.35794 ± 0.12105
k1	0.0508 ± 0.00521
n1	0.50545 ± 0.02498
q2	1.45872 ± 0.07732
k2	6.36825 ± 0.14248
n2	1.1794 ± 0.046
Reduced Chi-Sqr	5.41152E-5
R-Square (COD)	0.99995
Adj. R-Square	0.99994

Fig. S15 Dual-Site Langmuir-Freundlich (DSLF) model fitting of the *iso*-C_4H_8 isotherm of **1·K** at 298 K and 313 K.

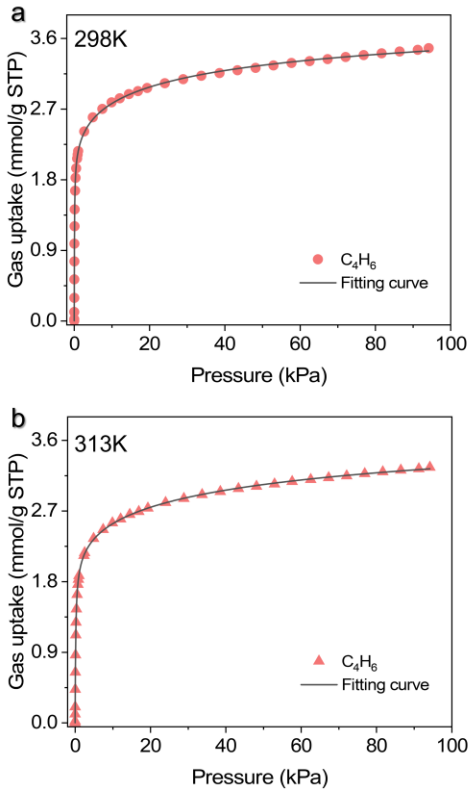

Model	DSLF (User)
Equation	q1*(k1*x)^n1/[1+(k1*x)^n1]+q2*(k2*x)^n2/[1+(k2*x)^n2]
q1	2.75545 ± 0.25702
k1	0.0392 ± 0.00762
n1	0.44101 ± 0.04154
q2	1.67745 ± 0.11918
k2	15.8782 ± 0.50156
n2	1.17848 ± 0.07267
Reduced Chi-Sqr	2.77713E-4
R-Square (COD)	0.9998
Adj. R-Square	0.99978

Model	DSLF (User)
Equation	q1*(k1*x)^n1/[1+(k1*x)^n1]+q2*(k2*x)^n2/[1+(k2*x)^n2]
q1	2.73312 ± 0.21136
k1	0.01909 ± 0.00345
n1	0.46335 ± 0.0336
q2	1.68726 ± 0.09045
k2	6.65474 ± 0.16539
n2	1.1047 ± 0.04502
Reduced Chi-Sqr	9.69686E-5
R-Square (COD)	0.99992
Adj. R-Square	0.99991

Fig. S16 Dual-Site Langmuir-Freundlich (DSLF) model fitting of the C_4H_6 isotherm of **1·K** at 298 K and 313 K.

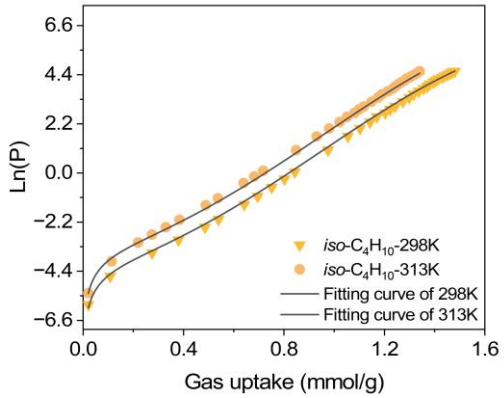

Model	Qstparameter (User)	
Equation	ln(x)+1/K*(a0+a1*x+a2*x^2+a3*x^3+a4*x^4)+(b0+b1*x+b2*x^2+b3*x^3)	
a0*	-4171.03755 ± 0	-4171.03755 ± 0
a1*	-86.74358 ± 0	-86.74358 ± 0
a2*	95.07175 ± 0	95.07175 ± 0
a3*	-83.94757 ± 0	-83.94757 ± 0
a4*	-29 ± 0	-29 ± 0
b0*	11.83513 ± 0.06201	11.83513 ± 0.06201
b1*	-1.97231 ± 0.32577	-1.97231 ± 0.32577
b2*	8.12782 ± 0.47373	8.12782 ± 0.47373
b3*	-2.29844 ± 0.19899	-2.29844 ± 0.19899
k	298 ± 0	313 ± 0
Reduced Chi-Sqr*	0.01043	
R-Square (COD)	0.99878	0.99886
R-Square (COD)*	0.99882	
Adj. R-Square*	0.99877	

Fig. S17 Virial fittings (lines) of *iso*-C_4H_{10} adsorption isotherms (symbols) of **1** at 298 K and 313 K.

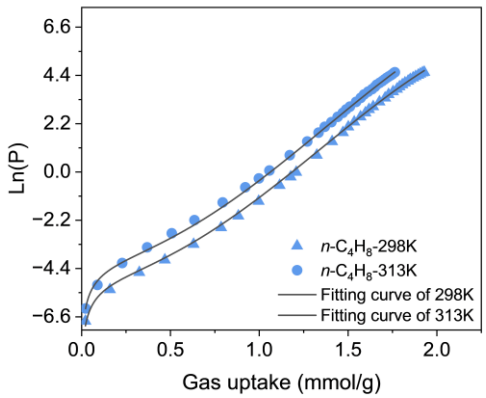

Model	Qstparameter (User)	
Equation	ln(x)+1/K*(a0+a1*x+a2*x^2+a3*x^3+a4*x^4)+(b0+b1*x+b2*x^2+b3*x^3)	
a0*	-4671.03755 ± 0	-4671.03755 ± 0
a1*	-162.4619 ± 0	-162.4619 ± 0
a2*	133.72796 ± 0	133.72796 ± 0
a3*	-80.37779 ± 0	-80.37779 ± 0
a4*	-29.58588 ± 0	-29.58588 ± 0
b0*	12.53389 ± 0.05222	12.53389 ± 0.05222
b1*	-1.82247 ± 0.22361	-1.82247 ± 0.22361
b2*	4.98714 ± 0.25265	4.98714 ± 0.25265
b3*	-0.73205 ± 0.08114	-0.73205 ± 0.08114
k	298 ± 0	313 ± 0
Reduced Chi-Sqr*	0.0081	
R-Square (COD)	0.99921	0.99921
R-Square (COD)*	0.99921	
Adj. R-Square*	0.99918	

Fig. S18 Virial fittings (lines) of *n*-C_4H_8 adsorption isotherms (symbols) of **1** at 298 K and 313 K.

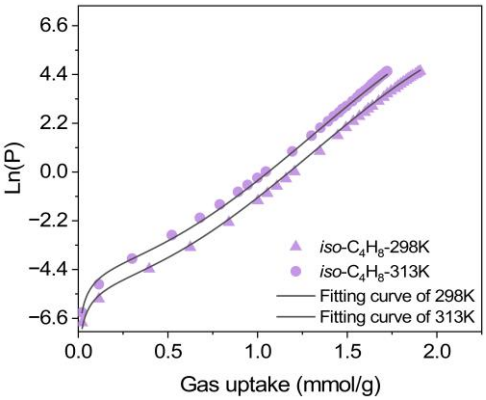

Model	Qstparameter (User)	
Equation	ln(x)+1/K*(a0+a1*x+a2*x^2+a3*x^3+a4*x^4)+(b0+b1*x+b2*x^2+b3*x^3)	
a0*	-4642.19267 ± 0	-4642.19267 ± 0
a1*	-151.15199 ± 0	-151.15199 ± 0
a2*	109.89413 ± 0	109.89413 ± 0
a3*	-57.27825 ± 0	-57.27825 ± 0
a4*	-30.05906 ± 0	-30.05906 ± 0
b0*	12.3891 ± 0.07058	12.3891 ± 0.07058
b1*	-2.13462 ± 0.30601	-2.13462 ± 0.30601
b2*	5.568 ± 0.35426	5.568 ± 0.35426
b3*	-0.9743 ± 0.11545	-0.9743 ± 0.11545
k	298 ± 0	313 ± 0
Reduced Chi-Sqr*	0.01435	
R-Square (COD)	0.99857	0.99851
R-Square (COD)*	0.99854	
Adj. R-Square*	0.99847	

Fig. S19 Virial fittings (lines) of *iso*-C_4H_8 adsorption isotherms (symbols) of **1** at 298 K and 313 K.

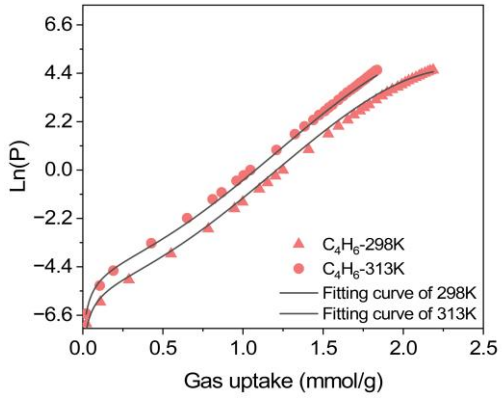

Model	Qstparameter (User)	
Equation	ln(x)+1/K*(a0+a1*x+a2*x^2+a3*x^3+a4*x^4)+(b0+b1*x+b2*x^2+b3*x^3)	
a0*	-4871.03755 ± 0	-4871.03755 ± 0
a1*	-86.74358 ± 0	-86.74358 ± 0
a2*	55.07175 ± 0	55.07175 ± 0
a3*	-43.94757 ± 0	-43.94757 ± 0
a4*	-29 ± 0	-29 ± 0
b0*	12.86531 ± 0.09845	12.86531 ± 0.09845
b1*	-1.53545 ± 0.37557	-1.53545 ± 0.37557
b2*	5.06555 ± 0.38235	5.06555 ± 0.38235
b3*	-0.97407 ± 0.1099	-0.97407 ± 0.1099
k	298 ± 0	313 ± 0
Reduced Chi-Sqr*	0.03327	
R-Square (COD)	0.99657	0.99712
R-Square (COD)*	0.99683	
Adj. R-Square*	0.99668	

Fig. S20 Virial fittings (lines) of C_4H_6 adsorption isotherms (symbols) of **1** at 298 K and 313 K.

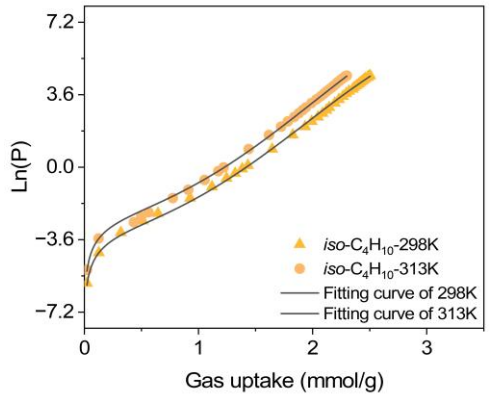

Model	Qstparameter (User)	
Equation	ln(x)+1/K*(a0+a1*x+a2*x^2+a3*x^3+a4*x^4)+(b0+b1*x+b2*x^2+b3*x^3)	
a0*	-4418.0784 ± 0	-4418.0784 ± 0
a1*	115.90637 ± 0	115.90637 ± 0
a2*	-121.49984 ± 0	-121.49984 ± 0
a3*	57.21964 ± 0	57.21964 ± 0
a4*	-33.62111 ± 0	-33.62111 ± 0
b0*	12.723 ± 0.05562	12.723 ± 0.05562
b1*	-1.31563 ± 0.18181	-1.31563 ± 0.18181
b2*	1.84227 ± 0.15943	1.84227 ± 0.15943
b3*	0.02801 ± 0.03976	0.02801 ± 0.03976
k	298 ± 0	313 ± 0
Reduced Chi-Sqr*	0.00984	
R-Square (COD)	0.99893	0.99863
R-Square (COD)*	0.99879	
Adj. R-Square*	0.99873	

Fig. S21 Virial fittings (lines) of *iso*-C_4H_{10} adsorption isotherms (symbols) of **1·K** at 298 K and 313 K.

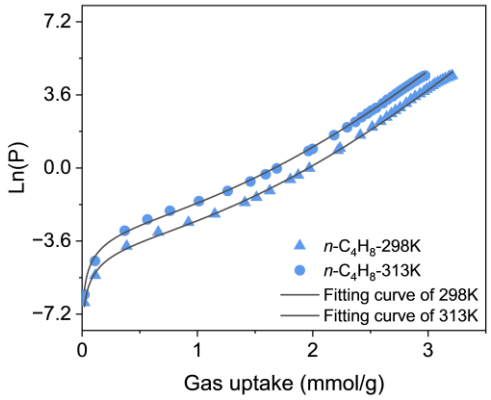

Model	Qstparameter (User)	
Equation	ln(x)+1/K*(a0+a1*x+a2*x^2+a3*x^3+a4*x^4)+(b0+b1*x+b2*x^2+b3*x^3)	
a0*	-5052.98844 ± 0	-5052.98844 ± 0
a1*	-406.65666 ± 0	-406.65666 ± 0
a2*	47.48727 ± 0	47.48727 ± 0
a3*	3.46226 ± 0	3.46226 ± 0
a4*	-1.6 ± 0	-1.6 ± 0
b0*	14.01329 ± 0.04959	14.01329 ± 0.04959
b1*	0.76573 ± 0.132	0.76573 ± 0.132
b2*	0.81612 ± 0.09221	0.81612 ± 0.09221
b3*	-0.04385 ± 0.01809	-0.04385 ± 0.01809
k	298 ± 0	313 ± 0
Reduced Chi-Sqr*	0.009	
R-Square (COD)	0.9989	0.99918
R-Square (COD)*	0.99903	
Adj. R-Square*	0.99898	

Fig. S22 Virial fittings (lines) of *n*-C_4H_8 adsorption isotherms (symbols) of **1·K** at 298 K and 313 K.

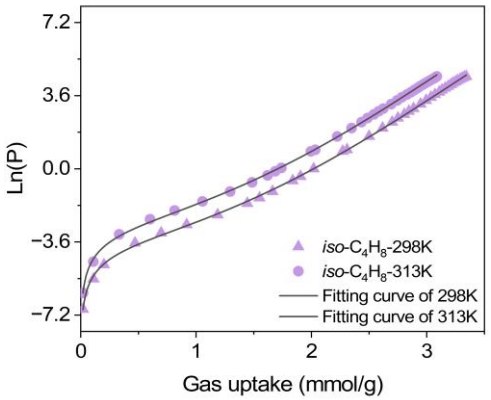

Model	Qstparameter (User)	
Equation	ln(x)+1/K*(a0+a1*x+a2*x^2+a3*x^3+a4*x^4)+(b0+b1*x+b2*x^2+b3*x^3)	
a0*	-5208.96759 ± 0	-5208.96759 ± 0
a1*	-208.41031 ± 0	-208.41031 ± 0
a2*	-57.9034 ± 0	-57.9034 ± 0
a3*	33.38368 ± 0	33.38368 ± 0
a4*	-5.8 ± 0	-5.8 ± 0
b0*	14.42878 ± 0.02928	14.42878 ± 0.02928
b1*	0.38733 ± 0.0765	0.38733 ± 0.0765
b2*	0.8813 ± 0.05187	0.8813 ± 0.05187
b3*	-0.05201 ± 0.00981	-0.05201 ± 0.00981
k	298 ± 0	313 ± 0
Reduced Chi-Sqr*	0.00354	
R-Square (COD)	0.99966	0.99959
R-Square (COD)*	0.99963	
Adj. R-Square*	0.99962	

Fig. S23 Virial fittings (lines) of *iso*-C_4H_8 adsorption isotherms (symbols) of **1·K** at 298 K and 313 K.

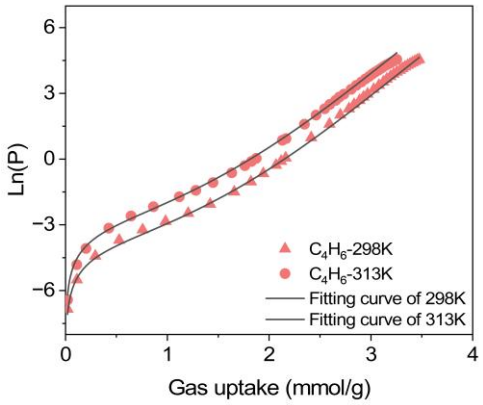

Model	Qstparameter (User)	
Equation	ln(x)+1/K*(a0+a1*x+a2*x^2+a3*x^3+a4*x^4)+(b0+b1*x+b2*x^2+b3*x^3)	
a0*	-5565.91591 ± 0	-5565.91591 ± 0
a1*	-468.8217 ± 0	-468.8217 ± 0
a2*	56.26952 ± 0	56.26952 ± 0
a3*	22.81274 ± 0	22.81274 ± 0
a4*	-5.6172 ± 0	-5.6172 ± 0
b0*	15.45931 ± 0.06663	15.45931 ± 0.06663
b1*	1.07788 ± 0.16916	1.07788 ± 0.16916
b2*	0.54282 ± 0.11064	0.54282 ± 0.11064
b3*	-0.02324 ± 0.02019	-0.02324 ± 0.02019
k	298 ± 0	313 ± 0
Reduced Chi-Sqr*	0.01917	
R-Square (COD)	0.99825	0.99791
R-Square (COD)*	0.99809	
Adj. R-Square*	0.99801	

Fig. S24 Virial fittings (lines) of C_4H_6 adsorption isotherms (symbols) of **1·K** at 298 K and 313 K.

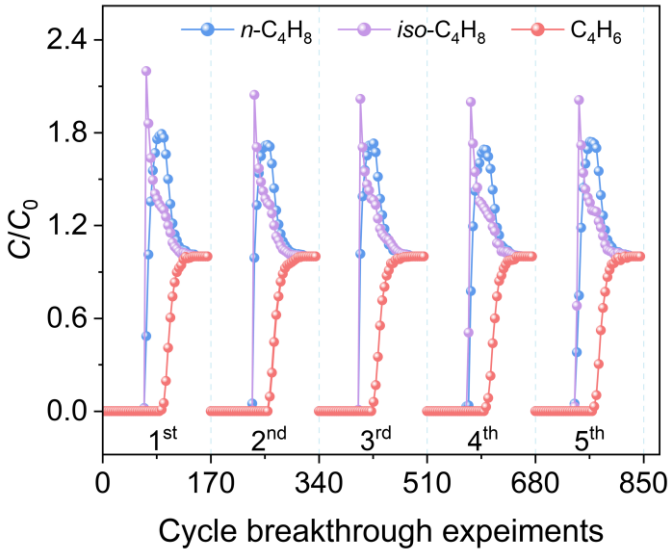

Fig. S25 Cycling breakthrough tests C_4H_6/*n*-C_4H_8/*iso*-C_4H_8 (1/1/1 (v/v /v)) with **1·K** at 298 K for five times.

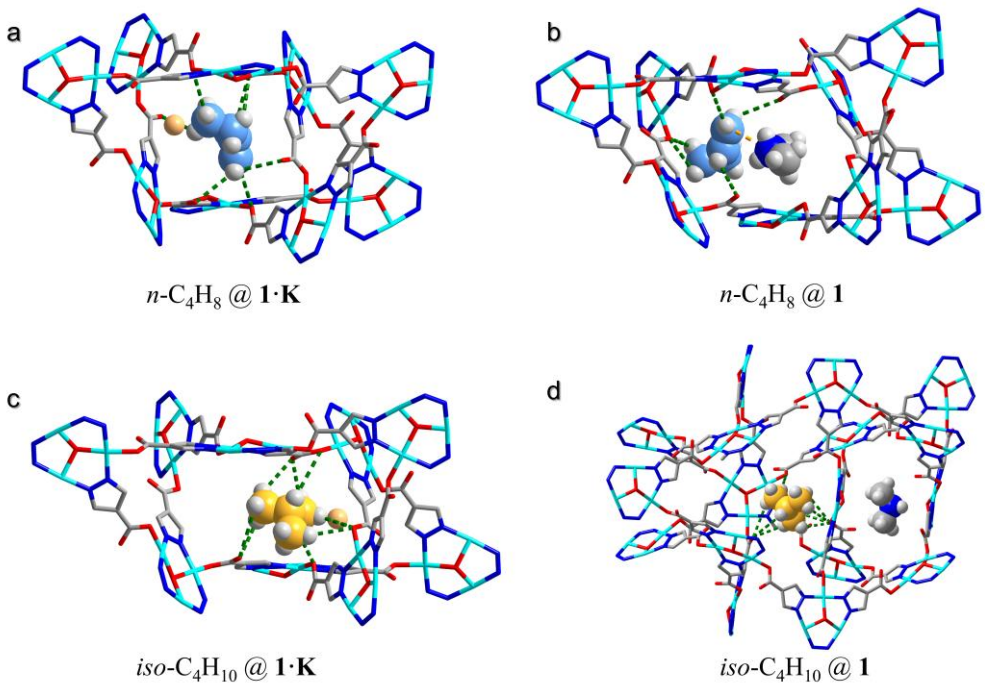

Fig. S26 The simulated binding structures of (a) *n*-C_4H_8@**1·K**, (b) *n*-C_4H_8@**1**, (c) *iso*-C_4H_{10}@**1·K** and (d) *iso*-C_4H_{10}@**1**. Color code: silver, C; white, H; red, O; blue, N; turquoise, Cu.

S3 Supplementary tables

Table S1 The physical properties of C4 olefins and paraffins.

Compound	Boiling point (K)	Kinetic diameter (Å)	Polarizability (Å^3)	Molecular size (Å^3)	Saturated vapor pressure (MPa) at 298 K	Dipole Moment (D)	Density (g/cm^3)	Concentration in C4 mixture (%)
C_4H_6	268.62	4.31	86.4	2.7×4.6×7.3	0.245	0.00	0.621	39.5
n-C_4H_8	266.92	4.46	79.7-85.2	3.5×4.5×7.4	0.247	0.359-0.438	0.595	13.0
iso-C_4H_8	266.25	4.84	80	3.6×5.2×6.0	0.256	0.550	0.594	27.2
iso-C_4H_{10}	261.34	5.28	81.4-82.9	4.5×5.5×6.2	0.288	0.132	0.557	3.6

Table S2 Separation performance comparison for materials at 298 K and 50 kPa

Materials	***iso*-C_4H_8 uptake (mmol g^{-1})**	***iso*-C_4H_{10} uptake (mmol g^{-1})**	**Uptake ratio**	**Refs**
HKUST-1	6.851	5.583	1.23	4
ZU-603	2.100	0.637	3.30	5
$[Cu_4(\mu_4\text{-}O)(\mu_2\text{-}OH)_2(Me_2trz\text{-}pba)_4]$	4.35[a]	3.83[c]	1.13	6
ZU-36-Co[c]	0.17	0.12	0.15	7
TIFSIX-3-Ni[c]	0.32	0.14	2.28	7
MIL-120[c]	2.16	1.71	1.26	7
$Zn(Hmpba)_2$[bd]	2.80	2.40	1.17	8
SD-65	0.029	0.022	1.29	9
Mn-bpdc	0.035	0.032	1.10	10
Ni-gallate	0.043	0.037	1.17	11
Mg-gallate	0.087	0.068	1.27	11
Co-gallate	0.106	0.093	1.14	11

Materials	*iso*-C_4H_8 uptake (mmol g^{-1})	*iso*-C_4H_{10} uptake (mmol g^{-1})	Uptake ratio	Refs
ZU-609	0.106	0.088	1.20	12
ZJNU-30a	5.364	7.556	0.71	13
1	1.78	1.37	1.30	**This work**
1·K	3.13	2.35	1.33	**This work**

a =103.4 kPa; b=101 kPa; c=100 kPa; d=303K.

Table S3 Comparison of uptake capacity and uptake selectivity of various adsorbents for C_4H_6/*n*-C_4H_8/*iso*-C_4H_8 at 298 K and 100 kPa.

Materials	Uptake (mmol g^{-1})			Uptake ratio		Refs
	C_4H_6	*n*-C_4H_8	*iso*-C_4H_8	C_4H_6/*n*-C_4H_8	C_4H_6/*iso*-C_4H_8	
ZJNU-30a	10.63	10.7	9.14	0.99	1.16	13
NOTT-101a[a]	9.28	9.28	9.15	1.00	1.00	14
ZJNU-80a[a]	8.35	8.35	6.80	1.00	1.23	14
SIFSIX-1-Cu[a]	6.75	6.43	6.28	1.10	1.13	15
TIFSIX-2-Cu-i[a]	4.00	3.67	2.90	1.09	1.38	15
SIFSIX-2-Cu-i[a]	3.99	3.06	1.74	1.30	2.29	15
Co-DOBDC	5.90	5.60	1.10	1.10	1.10	16
Zn-EIM-RHO	5.00	5.25	5.25	0.95	0.95	16
Zn-BTM[a]	2.70	1.71	1.73	1.21	1.19	16

Materials	Uptake (mmol g^{-1})			Uptake ratio		Refs
	C_4H_6	*n*-C_4H_8	*iso*-C_4H_8	C_4H_6/*n*-C_4H_8	C_4H_6/*iso*-C_4H_8	
SIFSIX-Cu-TPB	3.23	2.71	2.44	1.13	1.31	17
TIFSIX-Cu-TPB	3.35	2.96	2.56	1.13	1.31	17
$Zn(Hmpba)_2$[ad]	3.10	2.80	2.80	1.11	1.11	8
$Ni(pyz)Ni(CN)_4$	3.17	2.88	2.92	1.10	1.09	18
Y-fum-fcu-MOF[ad]	2.61	2.70	0.98	0.97	2.66	19
1[b]	2.19	1.93	1.91	1.13	1.14	**This work**
1·K[b]	3.48	3.21	3.34	1.08	1.04	**This work**

a =101 kPa; b=95 kPa; c=308K; d=303K.

References

1 B. Delley, From molecules to solids with the DMol^3 approach. *J. Chem. Phys.*, 2000, **113**, 7756-7764.

2 N. Metropolis, A. W. Rosenbluth, M. N. Rosenbluth, A. H. Teller, E. Teller, Equation of state calculations by fast computing machines. *J. Chem. Phys.*, 1953, **21**, 1087-1092.

3 A. K. Rappé, K. S. Colwell, C. J. Casewit, Application of a universal force field to metal complexes. *Inorg. Chem.*, 1993, **32**, 3438-3450.

4 M. Hartmann, S. Kunz, D. Himsl, O. Tangermann, Adsorptive separation of isobutene and isobutane on $Cu_3(BTC)_2$. *Langmuir*, 2008, **24**, 8634-8642.

5 Z. Qiu, J. Cui, D. Zhou, Z. Yang, X. Lu, X. Suo, A. Zhang, X. Cui, L. Yang, H. Xing, Efficient stacking of iso-butene in sulfonate functional metal-organic frameworks for efficient iso-butene/iso-butane separation. *Ind. Chem. Mater.*, 2025, **3**, 535-542.

6 M. Lange, M. Kobalz, J. Bergmann, D. Lässig, J. Lincke, J. Möllmer, A. Möller, J. Hofmann, H. Krautscheid, R. Staudt, R. Gläser, Structural flexibility of a copper-based metal–organic framework: sorption of C4-hydrocarbons and in situ XRD. *J. Mater. Chem. A*, 2014, **2**, 8075-8085.

7 Z. Zhang, B. Tan, P. Wang, X. Cui, H. Xing, Highly efficient separation of linear and branched C4 isomers with a tailor-made metal–organic framework. *AIChE Journal*, 2020, **66**.

8 Z.-M. Ye, C.-T. He, Y.-T. Xu, R. Krishna, Y. Xie, D.-D. Zhou, H.-L. Zhou, J.-P. Zhang, X.-M. Chen, A new isomeric porous coordination framework showing single-crystal to single-crystal structural transformation and preferential adsorption of 1,3-Butadiene from C_4 hydrocarbons. *Cryst. Growth Des.*, 2017, **17**, 2166-2171.

9 K. Kishida, Y. Okumura, Y. Watanabe, M. Mukoyoshi, S. Bracco, A. Comotti, P. Sozzani, S. Horike,

S. Kitagawa, Recognition of 1,3-Butadiene by a porous coordination polymer. *Angew. Chem. Int. Ed.*, 2016, **55**, 13784-13788.

10 W. Lu, H. Huang, Z. Hejin, C. Yanjiao, G. Xiangyu, Y. Fan, C. Zhong, Efficient separation of 1,3-butadiene from C4 hydrocarbons by flexible metal-organic framework with gate-opening effect. *AIChE Journal*, 2022, **68**, e17568.

11 J. Chen, J. Wang, L. Guo, L. Li, Q. Yang, Z. Zhang, Y. Yang, Z. Bao, Q. Ren, Adsorptive separation of geometric isomers of 2-Butene on gallate-based metal-organic frameworks. *ACS Appl. Mater. Interfaces.*, 2020, **12**, 9609-9616.

12 J. Cui, Z. Qiu, Z. Yang, A. Jin, X. Cui, L. Yang, H. Xing, One-step butadiene purification in a sulfonate-functionalized metal-organic framework through synergistic separation mechanism. *Angew. Chem. Int. Ed.*, 2024, **63**, e202403345.

13 H. Liu, Y. He, J. Jiao, D. Bai, D. l. Chen, R. Krishna, B. Chen, A porous zirconium-based metal-organic framework with the potential for the separation of butene isomers. *Chem. Eur. J.*, 2016, **22**, 14988-14997.

14 J. Jiao, H. Liu, D. Bai, Y. He, A chemically cross-linked NbO-type metal-organic framework: cage or window partition? *Inorg. Chem.*, 2016, **55**, 3974-3979.

15 Z. Zhang, Q. Yang, X. Cui, L. Yang, Z. Bao, Q. Ren, H. Xing, Sorting of C4 olefins with interpenetrated hybrid ultramicroporous materials by combining molecular recognition and size-sieving. *Angew. Chem. Int. Ed.*, 2017, **56**, 16282-16287.

16 P.-Q. Liao, N.-Y. Huang, W.-X. Zhang, J.-P. Zhang, X.-M. Chen, Controlling guest conformation for efficient purification of butadiene. *Science*, 2017, **356**, 1193-1196.

17 Y. Liu, Y. Zhang, P. Zhang, Y. Peng, X. Liu, J. Chen, S. Chen, Z. Zeng, J. Wang, S. Deng, Two novel

4,6-connected anion-pillared metal-organic frameworks for simultaneous separation of C_3 and C_4 olefins. *CHEM ENG PROCESS*, 2022, **172**, 108768.

18 J.-X. Chen, X.-X. Xiao, L. Li, J. Li, R.-B. Lin, X.-M. Chen, Fine-tuning of Hofmann-type metal-organic frameworks for highly efficient separation of C_4 olefins. *Chin. J. Struct. Chem.*, 2025, **44**, 100744.

19 A. H. Assen, T. Virdis, W. De Moor, A. Moussa, M. Eddaoudi, G. Baron, J. F. M. Denayer, Y. Belmabkhout, Kinetic separation of C_4 olefins using Y-fum-fcu-MOF with ultra-fine-tuned aperture size. *Chem. Eng. J.*, 2021, **413**, 127388.